

Investigating the Effect of Shading on the Capacity Factor of Floating Photovoltaic Systems

Ali Murat Ateş^{1*} , Osman Salih Yılmaz² , Fatih Gülgen³ 

¹Manisa Celal Bayar University, Faculty of Education 45900 Demirci, Manisa, Türkiye

²Manisa Celal Bayar University, Demirci Vocational School 45900 Demirci, Manisa, Türkiye

³Yıldız Technical University, Faculty of Civil Engineering, 34220 Esenler, İstanbul, Türkiye

* murat.ates@cbu.edu.tr

* Orcid: 0000-0002-2815-1404

Received: 6 November 2021

Accepted: 12 September 2022

DOI: 10.18466/cbayarfbe.1020070

Abstract

This study proposes a method to identify the most efficient regions for energy production before installing FPV on any water reservoir. Remote sensing (RS) was used to determine the 20-year area and shoreline changes of the Demirköprü Dam reservoir. The reservoir's annual and monthly total global horizontal irradiance (GHI) values were calculated based on 20 years of observations using a geographic information system (GIS) solar analysis tool. The regional theoretical capacity factor (RTCF) proposed in this study was modelled using total annual GHI values. The water surface was divided into four regions using RTCFs. 94.97%, 4.92%, 0.08% and 0.02% of the total water surface area were classified as RTCF21, RTCF20, RTCF19 and RTCF18, respectively. The annual electrical energy potentials per unit for each RTCF were calculated. The novel method developed in this study for determining the optimum location of FPV SPPs to be installed on water surfaces reveals the importance of evaluating land topography and considering annual shading patterns.

Keywords: Floating photovoltaic, geographical information system, regional theoretical capacity factor, remote sensing, solar analysis

1. Introduction

Photovoltaic (PV) solar power plants (SPPs) that convert solar energy into electrical energy are widely used in many countries. PV systems started to be used intensively in rural areas where electricity grid problems were experienced at first. However, recently, it has been frequently used to reduce economic costs and carbon emissions by supporting the electricity needed with solar energy. Even though their efficiency has increased with the new techniques developed recently, PV modules still work with around 20% efficiency. This shows that large areas are needed to install solar power plants.

Recent studies and practical applications show that solar panels are often installed on marginal agricultural lands, building facades, roofs, lakes, dams, canals, and offshore areas. Soil is an indispensable resource for humanity. Even if it has lost its ability to be cultivated, it can be used as settlement, forestation, or pasture.

Land occupation by PV SPPs causes land prices to rise sharply, especially in high-density urban residential areas. This adds additional costs to PV systems. On the other hand, installing PV modules on building roofs or façades may not always give the desired result due to the shading of surrounding buildings or objects such as trees. Using broad water surfaces to install PV systems has emerged as a new concept when all these factors are considered together.

FPV technology was first commissioned in Aichi, Japan, in 2007, with a capacity of 20 MW to facilitate research on solar power generation on water surfaces [1]. Rapidly increasing FPV SPPs worldwide have applications in countries such as China, India, the Republic of Korea, and Brazil [2]. One of the reasons for the rapid spread of FPV SPPs is the cooling effect of evaporating water. A decrease in module temperature can increase system efficiency and the amount of energy produced [3]. [4] observed that the front temperature of the FPV modules is 2–4% lower and the back

temperature is 5–11% lower compared to similar On Ground PV modules. Since FPV systems create shade on the water surface, the evaporation rate of the water is lowered by approximately 25–70% [5]. In addition to these advantages, FPV plants installed on freshwater surfaces also increase water quality by reducing algae growth and preventing eutrophication [6]. Due to all these advantages, the installed capacity of FPV in the world is growing exponentially every year.

Dam reservoirs, one of the surfaces where FPV systems can be installed, are a reliable water source for various applications. Water reservoirs generally have optimal conditions for FPV installation, such as constant water inlet and outlet, optimum temperature, and water availability for cleaning the modules [7]. In addition, the intermittent operation of the equivalent FPV system to meet the energy demand reduces the pressure on the power turbines in the hydroelectric power plant by removing some or all of the electricity generation load [1]. FPV systems are seen as an alternative that addresses increasing energy demand and contributes to the generation capacity of the existing hydroelectric power plants where they are installed without requiring additional land costs [8], [9].

The installation of FPVs should be planned considering the water dynamics of the region. Remote sensing (RS) offers the opportunity to rapidly and cost-effectively identify changes in reservoir size resulting from seasonal influences, agricultural irrigation, and power generation processes [10]. It is possible to determine the shoreline of a large dam reservoir's surface using medium-resolution images from free satellites such as Landsat and Sentinel [11]. The cloud-based Google Earth Engine (GEE) platform has been highly preferred recently. Google developed GEE to map human settlements in large areas, analyze past changes, and constantly update current estimates [12]. GEE can provide easy and simultaneous access to all archives of Landsat and Sentinel images. GEE, through its application program interface (API), allows development with JavaScript and Python coding languages and the ability to access and apply petabyte-scale data [13].

Regardless of the PV systems' surface installed, the most crucial parameter is the amount of total radiation falling on the module surface. Therefore, it is essential to evaluate solar sources by analyzing and predicting the spatiotemporal distribution of solar radiation [14]. In this planning, the slope of the modules, reflections, and shadows from the environment are the criteria to be considered separately. GIS, which includes spatial analysis and query methods, offers various tools such as Hillshade and Solar analysis for calculating shading. The solar radiation value can be calculated for a specific geographic location in certain periods using solar analysis tools that consider the shading effect [15].

Topographic factors such as height differences and slope changes that make up the land surface shapes in the region are the main factors used in calculating the shading effect and the amount of total solar radiation on the surface.

Many studies in the literature consider shading in the installation of PV SPPs in rural areas and on rooftop surfaces using GIS and RS techniques together. Some studies have focused on the three-dimensional modelling of roofs for appropriate placement of PV modules [16]–[18]. Several studies employed three-dimensional models using light detection and ranging (LIDAR) data, and the shading effect and other factors were evaluated together [19], [20]. In addition, digital surface models (DSMs) have been used to calculate the shading effects caused by the topography of the land [21], [22]. Some studies aimed to determine appropriate locations for PV SPP installation using GIS [23]–[25]. However, few studies have investigated the effects of shading on water surfaces for FPV system installation. [26] performed shading analysis using a fish-eye lens camera and a digital elevation model (DEM) in a mining lake in Korea. [27] suggested using RS and GIS techniques to increase the efficiency of FPV projects. [28] considered the shading effect of artificial elements around a lake in India on a 2 MW FPV system installed on the water surface. Determining the boundaries of the water surface on which an FPV-SPP will be installed to pinpoint the region with the highest efficiency is crucial for researchers and investors.

Revealing temporal changes to energy demands is critical to determining the renewable energy supply cost and calculating the capacity factor [29]. The capacity factor is an important indicator used in determining PV system performance. The capacity factor is the ratio of energy generated by a system over a given time to the energy generated by operating at nominal power for 24 hours a day [30]. In recent years, the trend toward electricity generation from wind and solar energy increased due to the developing technology and increasing capacity factors [31]. Capacity factors in coal, geothermal, hydroelectric, oil, natural gas, wind, and solar power plants used for electrical energy generation are 73%, 58%, 56%, 54%, 44%, 33%, and 20%, respectively [32]. This clearly shows how installing solar power plants, which produce at the lowest capacity factor than other systems, in proper areas can benefit the system's profitability.

This study proposes a novel method for projecting the energy to be obtained from FPV panels installed on the surface of a dam's reservoir. The developed method reveals the potential benefits of using RS and GIS technologies in solar resource assessment. The 20-year images of satellites are processed to determine the reservoir's shorelines properly. The GIS solar analysis tool offers the energy potential over the water surface.

The effect of shading on the capacity factor is assessed by calculating annual and monthly total irradiance per m^2 on the horizontal surface of the regions classified within the shorelines. The developed method results show that topographic factors around the planned area that cause shading effects must be considered before installing FPVs on water surfaces.

2. Study Area

The Köprübaşı district of Manisa Province, Turkey, where the Demirköprü Dam is located, is a rural area where people make their living from agriculture and animal husbandry.

The Demirköprü Dam was built between 1954 and 1960 for electricity generation, flood control, and agricultural irrigation (Figure 1). The Dam's volume, which is the earth-fill type, is approximately $4,300,000 m^3$. The average water level volume is $1,320 hm^3$. The reservoir surface area is about 3,000 ha depending on electricity generation, irrigation, and seasonal variables. The hydroelectric power plant, which has an installed power capacity of 69 MW, generates 193 GWh of electrical energy per year. It also provides irrigation services to an area of 99,220 ha.

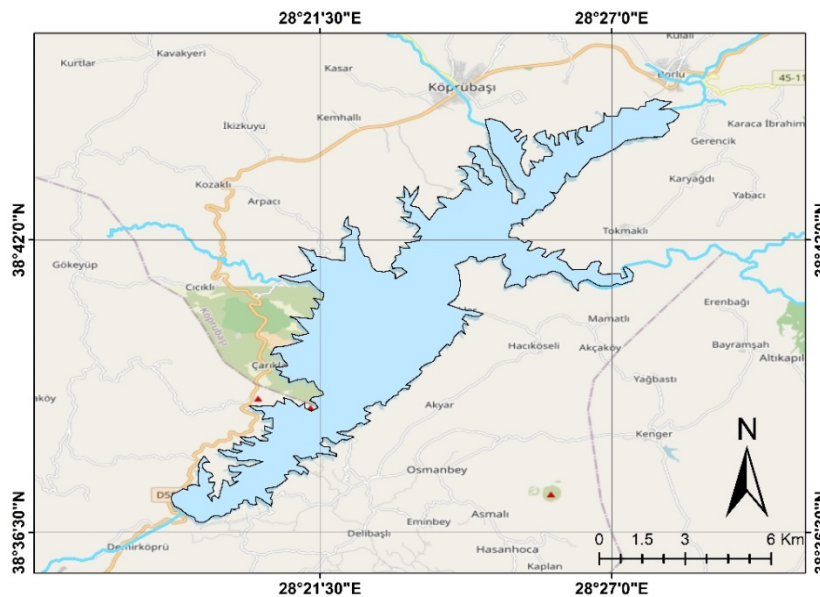


Figure 1. Location of the study area.

3. Method

3.1 Image Processing Method

Various algorithms and indices are used for image processing. Two basic approaches to classifying satellite images are supervised and unsupervised classification techniques. Classification approaches can be listed as pixel-based classification, sub-pixel classification, area-based classification, and object-based classification. Water surfaces can be differentiated from other details using pixel-based supervised classification algorithms and various extraction indices. The random forest (RF) algorithm and the normalized difference water index (NDWI) are examples of the algorithms and indices used herein. [33] applied maximum likelihood classification (MLC) and RF algorithms using Sentinel-2 (MSI) satellite images of the Demirköprü Dam in Turkey. Each algorithm used was tested separately on Sentinel-2 (MSI) images with visible (VIS) + infra-red band (NIR), normalized difference water index (NDWI), and modified normalized difference water index (MNDWI). The obtained images were compared

with producer's accuracy (PA), user's accuracy (UA), overall accuracy (OA), and Kappa statistics testing. As a result of comparisons based on classification accuracies, it was concluded that the RF algorithm performs better than the MLC algorithm for the Demirköprü Dam's reservoir.

In recent years, RF has been widely used in many fields such as medicine, economy and geography. [34] proposed RF, which changes the way a classification or regression tree is constructed. It has been proven to outperform many algorithms such as Support vector machine, k-nearest neighbours, and maximum likelihood classification, which make predictions by creating forests from RF decision trees [35]–[37].

[38] derived the Demirköprü Dam shoreline using the RF algorithm and NDWI water extraction indices (Eq. 3.1) on the GEE platform.

$$NDWI = (\rho_{Green} - \rho_{NIR}) / (\rho_{Green} + \rho_{NIR}) \quad (3.1)$$

3.2 Insolation Map Creation Method

Topography is an essential factor in determining the amount of solar energy falling on any surface on Earth. Solar radiation is affected by topographic factors such as elevation, aspect, slope, and shading. The spatial analyst tool provided by ArcGIS enables analysis of the total amount of radiation that falls on any surface on Earth over a given period. The ability to calculate the amount of radiation falling on the Dam's water surface provides excellent convenience in calculating the annual energy production and capacity factor of the FPV plant to be installed thereon. In this study, ArcGIS solar radiation tool was preferred to calculate the amount of solar radiation. The data obtained from the digital elevation model (DEM) of the 30-meter spatial resolution shuttle radar topography mission (SRTM) was used as the elevation model.

Although there are standard parameters in the solar Analysis tool, it is necessary to make some changes in the parameters depending on the atmospheric conditions. This tool's parameters were calibrated in this study considering the radiation data provided by PVGIS software, Era-5 and Merra-2 satellites according to the region's location. Topographic and radiation parameters are shown in Table 1.

Table 1. Solar radiation parameters used in this study.

Topographic parameters	
Z factor	1
Calculation directions	DEM
Calculation direction	16
Radiation parameters	
Zenith divisions	8
Azimuth divisions	8
Diffuse model type	Standard overcast sky
Diffuse Proportion	0.5
Transmittivity	0.5

3.3 Regional Theoretical Capacity Factor Calculation Method

The capacity factor is calculated using equation 3.2 as the ratio of the energy generated by the system in one year to the total energy generated if operating at full capacity, according to IEC 61724 [39].

$$CF = \frac{E_G}{24 * 365 * P_R} \quad (3.2)$$

where CF is the capacity factor, E_G is the annual energy generated by the system, and P_R is the rated output power of the system.

The output power of a PV module depends on the incident solar radiation on its surface and the PV cell temperature. PV modules operate at rated power under standard test conditions (STC: 1000 W/m² irradiance, 25°C ambient temperature, and 1.5 air mass). The module output power shows a positive correlation with the total solar radiation falling on its surface and a negative correlation with the cell temperature. PV module output power depending on cell temperature and solar radiation is calculated as shown in equation 3.3 [40].

$$P_{PV} = P_R \left(\frac{I_t}{I_{STC}} \right) [1 - \alpha_T (T_{cell} - T_{STC})] \quad (3.3)$$

where P_{PV} is module output power, P_R is rated power of the module, I_t is instantaneous total (direct + diffuse + reflected) solar radiation on the module surface, α_T is PV module temperature coefficient of power, and T_c is cell temperature. Since the α_T value in the equation usually has a too low value of 0.04%/°C, it can be ignored in practice; in this case, the temperature-independent output power of the module is calculated using equation 3.4.

$$P_{PV} = P_R \left(\frac{I_t}{I_{STC}} \right) \quad (3.4)$$

Because the total amount of hourly radiation in an area of 1 m² at any location on Earth is shown as GHI (Wh/m²), the total amount of annual radiation (GHI_a) falling in this area is calculated with equation 3.5.

$$GHI_a = \sum_{day=1}^{365} \sum_{hour=1}^{24} GHI_{(day,hour)} \quad (3.5)$$

The annual electrical energy generated by a horizontally positioned module is calculated with equation 3.6.

$$E_G = P_R \left(\frac{GHI_a}{I_{STC}} \right) \quad (3.6)$$

Accordingly, it can be said that the amount of energy generated by a horizontally positioned PV module in any region is directly related to the GHI in that region. Based on this, the capacity factor of the PV system can be calculated with the local GHI. When equation 3.6 and equation 1 are summed together, equation 3.7 is obtained.

$$CF = \frac{E_G}{24 * 365 * P_R} = \frac{P_R \left(\frac{GHI_a}{I_{STC}} \right)}{8760 * P_R} \quad (3.7)$$

When the necessary simplifications are made in the equation, it is seen that the capacity factor of the PV-SPP to be installed in a horizontal position in a region is directly related to the GHI in that region.

In this case, to express the highest possible capacity factor of an SPP to be installed in a horizontal position in an area, the concept of regional theoretical capacity factor (RTCF) can be used; the RTCF of a region can be calculated with the equation 3.8.

$$RTCF = \frac{GHI_a}{8760 * I_{STC}} \quad (3.8)$$

Using the annual total GHI values calculated with the ArcGIS solar analysis tool, the RTCF value of each pixel was calculated. The RTCF map of the water surface was created by reclassifying the calculated RTCF values to correspond to integer numbers. The area of each region on the reclassified map and the

average amount of the annual total GHI were calculated with ArcGIS software.

3.4 Floating Photovoltaic System Design

Although many methods are used as flotation elements in floating photovoltaic systems, the most accepted materials in the literature are high-density polyethylene (HDPE) materials [27]. In this study, the PV modules were horizontally placed on flotation elements made of HDPE material with an interlocking structure. Between strings of 2×20 modules, one-meter pathways were left for module cleaning, assembly of string inverters, maintenance, and easy intervention in case of malfunction. Each SPP consisting of 40 PV modules and a 12 kWp string inverter, covers an area of 91.84 m² (Figure 2).

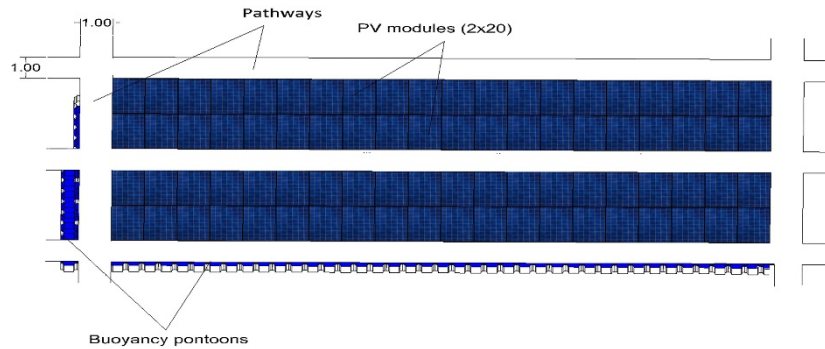


Figure 2. Designed FPV system.

The efficiency of the monocrystalline Axitec AC300M / 156-60S 300 W PV module used in the system is 18.44%, the temperature coefficient of Pmax is 0.42%/°C, and the module dimensions are 1640 × 992 mm. The maximum efficiency of the Huawei SUN 2000-12 KTL 12 kWp 3-phase string inverter is 98.5%, and the maximum number of power point trackers is 2.

3.5 Calculation of Annual Generated Electrical Energy

Total area and average annual total irradiance values in the region within the boundaries of each RTCF generated as a result of reclassification were calculated. The electrical energy potential generated from each RTCF region is calculated using equation 3.9 [41].

$$EGP_{RTCF} = A_{RTCF} \cdot R_{GHI} \cdot AF \cdot \eta_{PV} \quad (3.9)$$

where EGP_{RTCF} (GWh) is the energy potential that can be generated from an RTCF zone, A_{RTCF} (m²) is the total area of the zone, R_{GHI} (GWh/m²) is the average annual total GHI value per square meter in each region, AF (%) is the area factor, and η_{PV} (%) is the efficiency of the PV system. The AF in the formula is calculated by the ratio of total module surface area (A_{PV}) on the designed platform to the platform area (A_P) (Eq 3.10).

$$AF = \frac{A_{PV}}{A_P} \quad (3.10)$$

The efficiency of the PV GES system is calculated by multiplying the efficiency of all components in the system (Eq 3.11).

$$\eta_{sys} = \eta_m \cdot \eta_{cable} \cdot \eta_{inv} \cdot \eta_T \cdot (1 - Losses) \quad (3.11)$$

η_m = module efficiency (18.44% from manufacturer's datasheet)

η_{cable} = cable and junction box efficiencies (99.4%) [42]

η_{inv} = average inverter efficiency (98%)

η_T = transformer efficiency (97%) [42]

$Losses$ = total losses (7% temperature, low irradiance, and others)

4. Results

4.1 Satellite classification

The lowest water surface area reported of the Demirköprü Dam's reservoir was 1,562.45 ha by [38] (Figure 3).

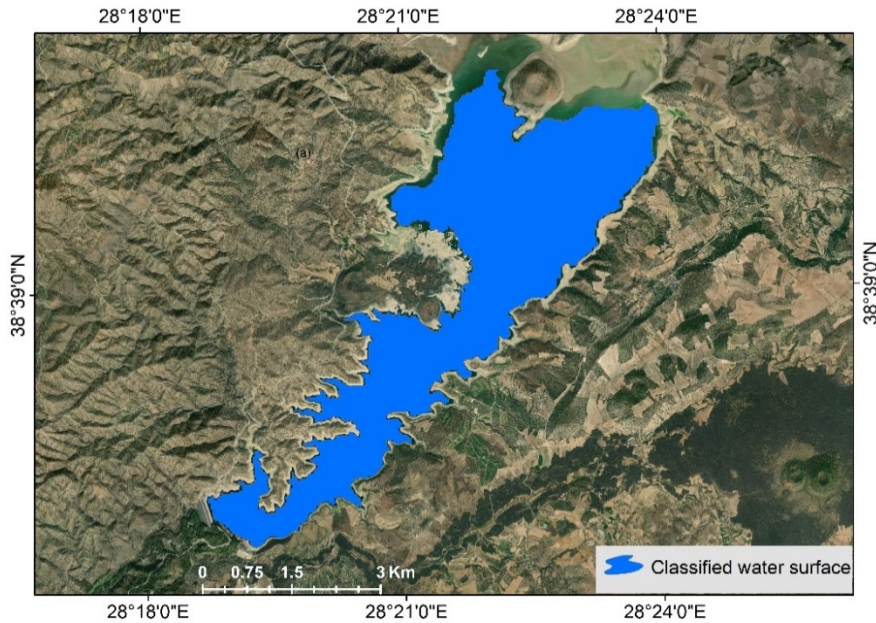


Figure 3. Lowest water surface.

The 10 m spatial resolution Sentinel satellite image dated 02.09.2018, the day when the water surface area was the lowest, was classified with RS and the islands detected on the water surface were marked with a red ellipse (Figure 4). The total area of the islands, consisting of sharp rocks, was calculated as 0.91 ha. The islands emerge in August and September when the

water level is low and disappear in February and March when the water level rises. Since the FPV SPP systems to be installed in this area would be damaged by receding water levels, the design must take these rocky islands into account.

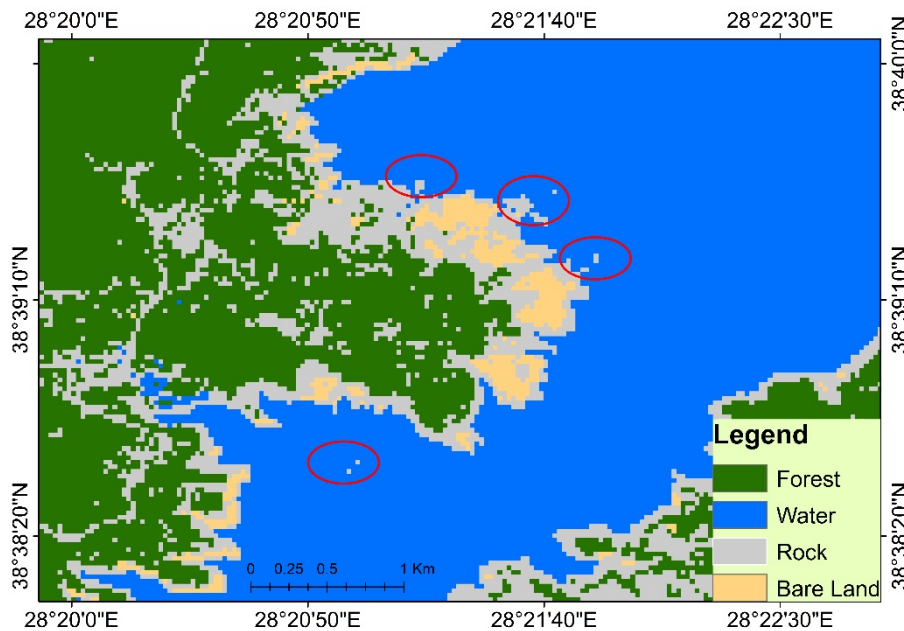


Figure 4. Islands composed of rock.

4.2 Regional Theoretical Capacity Factors

The total annual GHI for 2020 was calculated for each pixel in the area of the lowest water level in the Demirköprü Dam reservoir. The lowest and highest total annual GHIs calculated on the water surface were

1,553.96 kWh/m² and 1,875.25 kWh/m², respectively. In these GHI intervals, RTCF values were found to vary between 18% and 21%, and a class was created for each percentage. The minimum, maximum, and average values of total annual GHI for each RTCF class are shown in Table 2.

Table 2. RTCF classes and minimum, maximum, and average values of total annual GHI.

Zone	RTCF21	RTCF20	RTCF19	RTCF18
RTCF (%)	21	20	19	18
GHI Range (kWh/m ² -year)	1795.80 1875.25	1708.74 1795.79	1633.15 1705.68	1553.96 1606.82
Average of Regional Annual Total GHI (kWh/m ² -year)	1798.36	1790.85	1678.54	1576.19

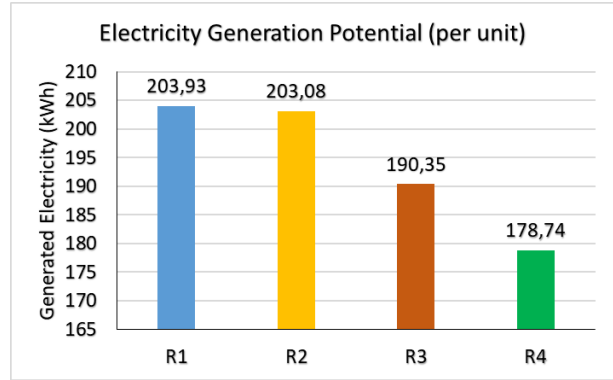


Figure 5. The potential electrical energy generated from an area of 1m² in each region.

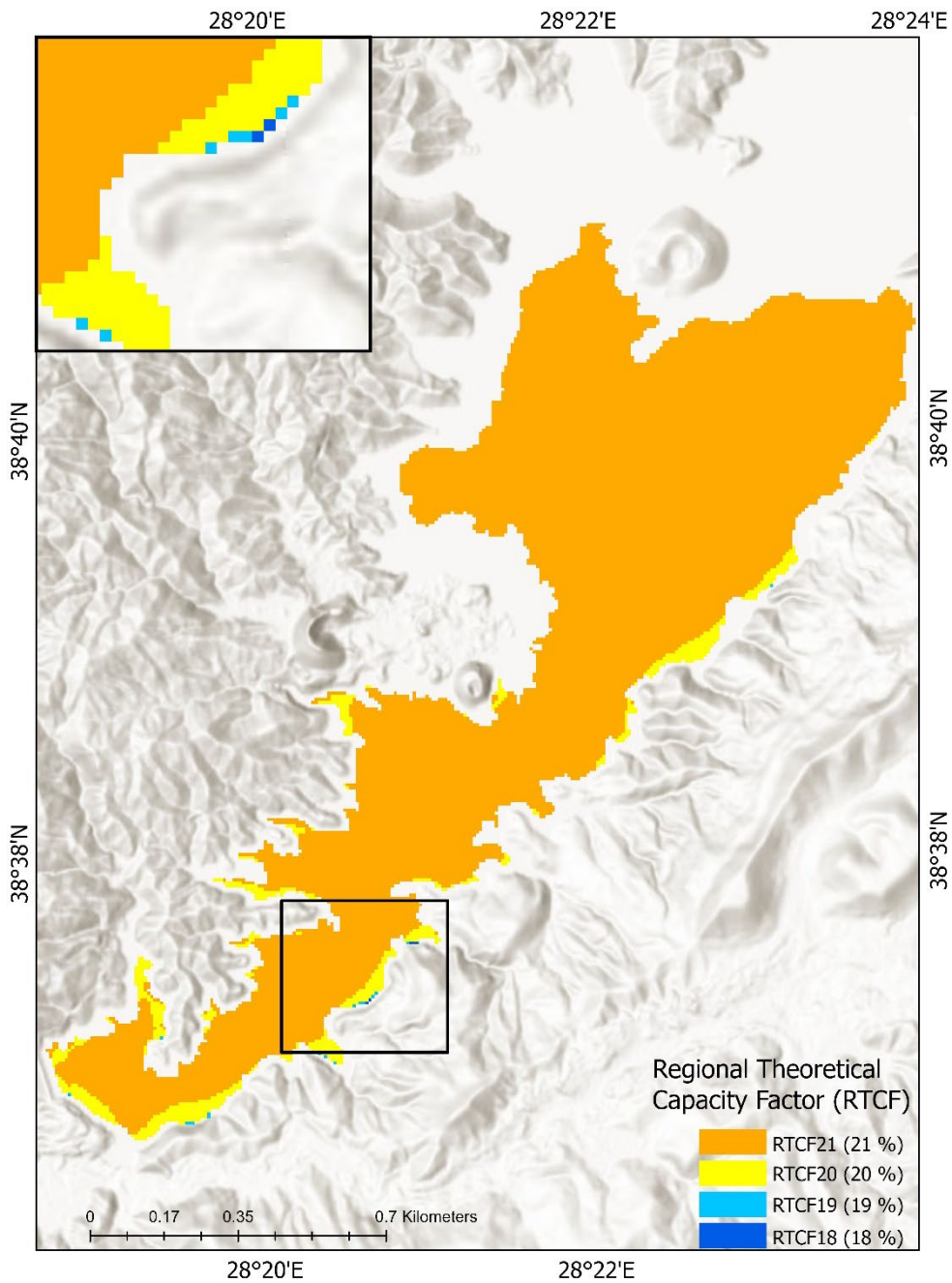


Figure 6. RTCF map.

The Table 2 shows that the average regional total annual GHI values of RTCF21 and RTCF20 are very similar, but RTCF19 and RTCF18 are lower by about 220 kWh/m² than RTCF21.

The total efficiency (η_{sys}) of the FPV system to be installed on the reservoir's surface was calculated as 16.20% using equation 11, and the area factor (AF) value of the designed floating platform was 0.7 using equation 10. Under these conditions, the potential annual electricity generation of 1 m² unit surface in each region was calculated and is shown in Figure 5.

According to the graph, while the potential of generating electricity from solar energy on the unit surface is above 200 kWh/year in RTCF21 and RTCF20 regions, it is 190 kWh/year in RTCF19 and 178 kWh/year in RTCF18. According to these values, RTCF21 and RTCF20 were more efficient for FPV installation than in the other regions.

The regional theoretical capacity factor map obtained using the four RTCF regions detected on the water surface is given in Figure 6.

As noted in Figure 4, a massive part of the water surface is classified as having an RTCF value of 21%. In areas close to the reservoir's shoreline, the RTCF value decreases to 20%. RTCF values of 19% and 18% were observed in a small area in the southern parts of the reservoir. The surface areas of each region were calculated with ArcGIS software. The small islands with an area of 0.91 ha determined in Figure 4 were subtracted from the total size of RTCF21. The total area of each region was multiplied by the region's potential electricity generation, and each region's real electricity generation potential was calculated and shown in Table 3.

Table 3. Area of regions.

Zone	Area (ha)	EGP (GWh)
RTCF21	1,482.95	3,024.24
RTCF20	76.9	156.17
RTCF19	1.3	2.47
RTCF18	0.38	0.68
Total	1,561.53	3,183.57

Monthly minimum, maximum, and average distributions of total annual GHI values calculated for each region are given in Table 4.

In January, when total radiation was lowest, the regional average monthly GHI values in RTCF21, RTCF20, RTCF19, and RTCF18 regions were calculated as 57.29 kWh/m², 56.80 kWh/m², 46.77 kWh/m², and 40.41 kWh/m², respectively. In July, at the highest radiation,

Table 4. Regional averages of monthly total GHI (kWh/m²)

	GHI	Regions			
		RTCF 21	RTCF 20	RTCF 19	RTCF 18
Jan.	Min	57.03	40.58	36.14	35.91
	Max	65.46	57.70	51.32	45.01
	Avg.	57.29	56.80	46.77	40.41
Feb.	Min	95.46	87.79	81.27	75.98
	Max	104.87	95.82	90.99	80.29
	Avg.	95.70	95.13	85.75	77.59
Mar.	Min	152.47	142.97	135.02	129.16
	Max	162.64	152.55	148.77	133.41
	Avg.	152.77	152.04	141.21	130.75
Apr.	Min	170.02	162.09	154.94	149.60
	Max	177.10	170.11	167.06	152.77
	Avg.	170.26	169.66	160.42	150.79
May	Min	203.36	201.65	194.90	190.62
	Max	210.74	207.81	204.22	192.43
	Avg.	207.94	207.39	199.70	191.33
Jun.	Min	206.43	208.75	202.40	199.28
	Max	214.83	213.60	209.96	200.16
	Avg.	213.73	213.21	206.87	199.75
Jul.	Min	239.06	241.09	233.71	229.62
	Max	249.23	247.21	241.96	231.02
	Avg.	247.43	246.70	238.71	230.22
Aug.	Min	213.78	207.91	200.39	194.61
	Max	221.62	216.08	211.38	197.43
	Avg.	216.30	215.54	205.76	195.67
Sep.	Min	161.82	152.63	144.87	139.04
	Max	171.07	161.86	158.12	143.11
	Avg.	162.07	161.36	150.87	140.57
Oct.	Min	113.28	104.63	97.27	91.60
	Max	123.63	113.54	109.23	96.16
	Avg.	113.53	112.88	102.67	93.32
Nov.	Min	88.58	76.13	69.82	68.18
	Max	96.74	88.91	82.03	75.11
	Avg.	88.92	88.30	78.23	71.63
Dec.	Min	71.87	50.77	50.14	50.27
	Max	79.33	72.46	66.47	59.91
	Avg.	72.42	71.83	61.58	54.15

these values were 247.43 kWh/m², 246.70 kWh/m², 238.71 kWh/m², and 230.22 kWh/m², respectively. This situation is related to the climatic conditions in the area. The lowest monthly total GHI value in RTCF21 was 71.87 kWh/m² in December, when the sun's altitude

angle (α) was the lowest, while it was 50.27 kWh/m² in RTCF18. In June, when the α angle was highest, the lowest monthly total GHI values in RTCF21 and RTCF18 regions were 206.43 kWh/m² and 199.28 kWh/m², respectively. It was observed that the difference between RTCF21 and RTCF18 in December was 21.60 kWh/m² and 7.14 kWh/m² in June. The monthly total GHI loss in the RTCF18 region due to shading was calculated as 30% in December and 4% in June. The effect of topography and α angle on the shading on the water surface, and thus on total GHI, is higher in the winter due to the lower α angle and lower in summer due to the higher α angle.

5. Conclusion

This study proposes a new method considering the importance of land topography and shading to determine the optimum location of FPV SPPs installed on water surfaces. The shading effect of the land topography on the water surface was carried out with the solar analysis tool using the DEM data of the land. As a result of the research, the annual and monthly total GHI values of each pixel in the satellite images were calculated. It has been observed that the RTCF values of the areas on the water surface vary between 18% and 21%.

Demirköprü Dam was chosen as the pilot area in this study. It is seen that the shoreline of the study area is shallow, and there are no high hills around it. Therefore, it was observed that the capacity factor decreased only in a tiny place with ridges on the south side. Total monthly GHI analysis was performed with the ArcGIS solar analysis tool to reveal the effect of the land topography and the sun's elevation angle (α) on shading and total annual GHI. The difference between the lowest GHI values of the RTCF21 and RTCF18 regions indicates that the monthly total GHI loss due to shading in the RTCF18 region was 30% in December and 4% in June.

In this study area, where the coastline is shallow, the shading effect of the topography is clearly visible. In addition, it is understood that the shading effect will be much more significant in the topography, where the terrain is wavy. The necessity of investigating the shading effect on water surfaces as well as in terrestrial systems has been demonstrated by this study. In this study, the horizontal variation of the water surface is considered, but it is recommended to investigate the effect of the vertical variation of the water on the shading.

Acknowledgement

This research did not receive any specific grant from funding agencies in the public, commercial, or not-for-

profit sectors and it was prepared from a part of author Osman Salih YILMAZ's Phd thesis.

Author's Contributions

Ali Murat Ateş: Drafted and wrote the energy analysis part and determined the simulation parameters. Assisted in the result interpretation and helped in manuscript preparation.

Osman Salih Yilmaz: Drafted and wrote the RS and GIS parts. He did the simulation. Assisted in the result interpretation and helped in manuscript preparation.

Fatih Gulgen: Planned and managed the RS and GIS parts. Assisted in the result interpretation and helped in manuscript preparation.

Ethics

There are no ethical issues after the publication of this manuscript.

References

- [1]. R. Nagananthini and R. Nagavinothini, "Investigation on floating photovoltaic covering system in rural Indian reservoir to minimize evaporation loss," *Int. J. Sustain. Energy*, vol. 40, no. 8, pp. 781–805, Sep. 2021, doi: 10.1080/14786451.2020.1870975.
- [2]. M. Tina, F. Bontempo Scavo, L. Merlo, and F. Bizzarri, "Analysis of water environment on the performances of floating photovoltaic plants," *Renew. Energy*, vol. 175, pp. 281–295, 2021, doi: 10.1016/j.renene.2021.04.082.
- [3]. G. Mamatha and P. S. Kulkarni, "Assessment of floating solar photovoltaic potential in India's existing hydropower reservoirs," *Energy Sustain. Dev.*, vol. 69, pp. 64–76, Aug. 2022, doi: 10.1016/j.esd.2022.05.011.
- [4]. H. Nisar, A. Kashif Janjua, H. Hafeez, S. Shakir, N. Shahzad, and A. Waqas, "Thermal and electrical performance of solar floating PV system compared to on-ground PV system-an experimental investigation," *Sol. Energy*, vol. 241, no. March, pp. 231–247, Jul. 2022, doi: 10.1016/j.solener.2022.05.062.
- [5]. A. El Hammoumi, A. Chalh, A. Allouhi, S. Motahhir, A. El Ghzizal, and A. Derouich, "Design and construction of a test bench to investigate the potential of floating PV systems," *J. Clean. Prod.*, vol. 278, p. 123917, 2021, doi: 10.1016/j.jclepro.2020.123917.
- [6]. R. Claus and M. López, "Key issues in the design of floating photovoltaic structures for the marine environment," *Renew. Sustain. Energy Rev.*, vol. 164, no. March, p. 112502, Aug. 2022, doi: 10.1016/j.rser.2022.112502.
- [7]. H. Rauf, M. S. Gull, and N. Arshad, "Integrating Floating Solar PV with Hydroelectric Power Plant: Analysis of Ghazi Barotha Reservoir in Pakistan," *Energy Procedia*, vol. 158, pp. 816–821, Feb. 2019, doi: 10.1016/j.egypro.2019.01.214.
- [8]. I. S. Rodrigues, G. L. B. Ramalho, and P. H. A. Medeiros, "Potential of floating photovoltaic plant in a tropical reservoir in Brazil," *J. Environ. Plan. Manag.*, vol. 63, no. 13, pp. 2334–2356, 2020, doi: 10.1080/09640568.2020.1719824.
- [9]. S. Sulaeman, E. Brown, R. Quispe-Abad, and N. Müller, "Floating PV system as an alternative pathway to the amazon dam underproduction," *Renew. Sustain. Energy Rev.*, vol. 135, no. July 2020, p. 110082, Jan. 2021, doi: 10.1016/j.rser.2020.110082.



- [10]. M. Arekhi, C. Goksel, F. Balik Sanli, and G. Senel, "Comparative Evaluation of the Spectral and Spatial Consistency of Sentinel-2 and Landsat-8 OLI Data for Igneada Longos Forest," *ISPRS Int. J. Geo-Information*, vol. 8, no. 2, p. 56, 2019, doi: 10.3390/ijgi8020056.
- [11]. X. Yang, S. Zhao, X. Qin, N. Zhao, and L. Liang, "Mapping of urban surface water bodies from sentinel-2 MSI imagery at 10 m resolution via NDWI-based image sharpening," *Remote Sens.*, vol. 9, no. 6, pp. 1–19, 2017, doi: 10.3390/rs9060596.
- [12]. N. N. Patel *et al.*, "Multitemporal settlement and population mapping from Landsat using Google Earth Engine," *Int. J. Appl. Earth Obs. Geoinf.*, vol. 35, no. PB, pp. 199–208, Mar. 2015, doi: 10.1016/j.jag.2014.09.005.
- [13]. R. Goldblatt, W. You, G. Hanson, and A. Khandelwal, "Detecting the Boundaries of Urban Areas in India: A Dataset for Pixel-Based Image Classification in Google Earth Engine," *Remote Sens.*, vol. 8, no. 8, p. 634, Aug. 2016, doi: 10.3390/rs8080634.
- [14]. Y. Choi, "Solar Power System Planning and Design," *Appl. Sci.*, vol. 10, no. 1, p. 367, Jan. 2020, doi: 10.3390/app10010367.
- [15]. Y. Charabi and A. Gastli, "GIS assessment of large CSP plant in Duqum, Oman," *Renew. Sustain. Energy Rev.*, vol. 14, no. 2, pp. 835–841, 2010.
- [16]. H. Jiang *et al.*, "Geospatial assessment of rooftop solar photovoltaic potential using multi-source remote sensing data," *Energy AI*, vol. 10, no. July, p. 100185, Nov. 2022, doi: 10.1016/j.egyai.2022.100185.
- [17]. S. Lin *et al.*, "Accurate Recognition of Building Rooftops and Assessment of Long-Term Carbon Emission Reduction from Rooftop Solar Photovoltaic Systems Fusing GF-2 and Multi-Source Data," *Remote Sens.*, vol. 14, no. 3144, Jun. 2022, doi: 10.3390/rs14133144.
- [18]. B. Chen, Y. Che, J. Wang, H. Li, L. Yu, and D. Wang, "An estimation framework of regional rooftop photovoltaic potential based on satellite remote sensing images," *Glob. Energy Interconnect.*, vol. 5, no. 3, pp. 281–292, Jun. 2022, doi: 10.1016/j.gloei.2022.06.006.
- [19]. X. Huang, K. Hayashi, T. Matsumoto, L. Tao, Y. Huang, and Y. Tomino, "Estimation of Rooftop Solar Power Potential by Comparing Solar Radiation Data and Remote Sensing Data—A Case Study in Aichi, Japan," *Remote Sens.*, vol. 14, no. 1742, Apr. 2022, doi: 10.3390/rs14071742.
- [20]. V. Stack and L. L. Narine, "Sustainability at Auburn University: Assessing Rooftop Solar Energy Potential for Electricity Generation with Remote Sensing and GIS in a Southern US Campus," *Sustainability*, vol. 14, no. 626, Jan. 2022, doi: 10.3390/su14020626.
- [21]. L. Romero Rodríguez, E. Duminił, J. Sánchez Ramos, and U. Eicker, "Assessment of the photovoltaic potential at urban level based on 3D city models: A case study and new methodological approach," *Sol. Energy*, vol. 146, pp. 264–275, 2017, doi: 10.1016/j.solener.2017.02.043.
- [22]. M. Aslani and S. Seipel, "Automatic identification of utilizable rooftop areas in digital surface models for photovoltaics potential assessment," *Appl. Energy*, vol. 306, no. 118033, Jan. 2022, doi: 10.1016/j.apenergy.2021.118033.
- [23]. Villacreses, J. Martínez-Gómez, D. Jijón, and M. Cordovez, "Geolocation of photovoltaic farms using Geographic Information Systems (GIS) with Multiple-criteria decision-making (MCDM) methods: Case of the Ecuadorian energy regulation," *Energy Reports*, vol. 8, pp. 3526–3548, Nov. 2022, doi: 10.1016/j.egyr.2022.02.152.
- [24]. B. Elboshy, M. Alwetaishi, R. M. H. Aly, and A. S. Zalhaf, "A suitability mapping for the PV solar farms in Egypt based on GIS-AHP to optimize multi-criteria feasibility," *Ain Shams Eng. J.*, vol. 13, no. 101618, May 2022, doi: 10.1016/j.asej.2021.10.013.
- [25]. S. Zambrano-Asanza, J. Quiros-Tortos, and J. F. Franco, "Optimal site selection for photovoltaic power plants using a GIS-based multi-criteria decision making and spatial overlay with electric load," *Renew. Sustain. Energy Rev.*, vol. 143, no. 110853, Jun. 2021, doi: 10.1016/j.rser.2021.110853.
- [26]. J. Song and Y. Choi, "Analysis of the Potential for Use of Floating Photovoltaic Systems on Mine Pit Lakes: Case Study at the Ssangyong Open-Pit Limestone Mine in Korea," *Energies*, vol. 9, no. 2, p. 102, Feb. 2016, doi: 10.3390/en9020102.
- [27]. A. Sahu, N. Yadav, and K. Sudhakar, "Floating photovoltaic power plant: A review," *Renew. Sustain. Energy Rev.*, vol. 66, pp. 815–824, 2016, doi: 10.1016/j.rser.2016.08.051.
- [28]. M. Abid, Z. Abid, J. Sagin, R. Murtaza, D. Sarbassov, and M. Shabbir, "Prospects of floating photovoltaic technology and its implementation in Central and South Asian Countries," *Int. J. Environ. Sci. Technol.*, vol. 16, no. 3, pp. 1755–1762, Mar. 2019, doi: 10.1007/s13762-018-2080-5.
- [29]. N. Mattsson, V. Verendel, F. Hedenus, and L. Reichenberg, "An autopilot for energy models – Automatic generation of renewable supply curves, hourly capacity factors and hourly synthetic electricity demand for arbitrary world regions," *Energy Strateg. Rev.*, vol. 33, p. 100606, Jan. 2021, doi: 10.1016/j.esr.2020.100606.
- [30]. A. Goswami and P. K. Sadhu, "Degradation analysis and the impacts on feasibility study of floating solar photovoltaic systems," *Sustain. Energy, Grids Networks*, vol. 26, p. 100425, 2021, doi: 10.1016/j.segan.2020.100425.
- [31]. P. A. Adedeji, S. A. Akinlabi, N. Madushele, and O. O. Olatunji, "Neuro-fuzzy resource forecast in site suitability assessment for wind and solar energy: A mini review," *J. Clean. Prod.*, vol. 269, p. 122104, 2020, doi: 10.1016/j.jclepro.2020.122104.
- [32]. P. A. Trotter, R. Maconachie, and M. C. McManus, "Solar energy's potential to mitigate political risks: The case of an optimized Africa-wide network," *Energy Policy*, vol. 117, no. March, pp. 108–126, 2018, doi: 10.1016/j.enpol.2018.02.013.
- [33]. O. S. Yılmaz, F. Gülgen, F. Balık Şanlı, and A. M. Ateş, "Demirköprü Barajının Su Yüzey Sınırlarının Belirlenmesinde Sentinel-2 (MSI) Görüntüleri Kullanılarak Farklı Algoritmalar ve Su Endeksleri Performanslarının Araştırılması," in *Hezarfen International Science, Mathematics, and Engineering Sciences Congress*, 2019, pp. 293–305.
- [34]. L. Breiman, "Random Forests," *Mach. Learn.*, vol. 45, pp. 5–32, 2001, doi: 10.1023/A:1010933404324.
- [35]. Y. Jin, X. Liu, Y. Chen, and X. Liang, "Land-cover mapping using Random Forest classification and incorporating NDVI time-series and texture: a case study of central Shandong," *Int. J. Remote Sens.*, vol. 39, no. 23, pp. 8703–8723, Dec. 2018, doi: 10.1080/01431161.2018.1490976.
- [36]. Y. He, C. Wang, F. Chen, H. Jia, D. Liang, and A. Yang, "Feature comparison and optimization for 30-M winter wheat mapping based on Landsat-8 and Sentinel-2 data using random forest algorithm," *Remote Sens.*, vol. 11, no. 5, 2019, doi: 10.3390/rs11050535.
- [37]. T. Noi Phan, V. Kuch, and L. W. Lehnert, "Land cover classification using google earth engine and random forest classifier—the role of image composition," *Remote Sens.*, vol. 12, no. 15, 2020, doi: 10.3390/RS12152411.
- [38]. A. M. Ates, O. S. Yılmaz, and F. Gülgen, "Using remote sensing to calculate floating photovoltaic technical potential of a dam's surface," *Sustain. Energy Technol. Assessments*, vol. 41, no. July, p.



100799, 2020, doi: 10.1016/j.seta.2020.100799.

[39]. M. Mwanza and K. Ulgen, *GIS-Based Assessment of Solar Energy Harvesting Sites and Electricity Generation Potential in Zambia*. 2021.

[40]. A. M. Ates and H. Singh, "Rooftop solar Photovoltaic (PV) plant – One year measured performance and simulations," *J. King Saud Univ. - Sci.*, vol. 33, no. 3, p. 101361, 2021, doi: 10.1016/j.jksus.2021.101361.

[41]. A. Gerbo, K. V. Suryabhagavan, and T. Kumar Raghuvanshi, "GIS-based approach for modeling grid-connected solar power potential sites: a case study of East Shewa Zone, Ethiopia," *Geol. Ecol. Landscapes*, vol. 00, no. 00, pp. 1–15, 2020, doi: 10.1080/24749508.2020.1809059.

[42]. E. Ghiani, F. Pilo, and S. Cossu, "Evaluation of photovoltaic installations performances in Sardinia," *Energy Convers. Manag.*, vol. 76, pp. 1134–1142, Dec. 2013, doi: 10.1016/j.enconman.2013.09.012.